

On the Collapse of Charged Scalar Fields

Yonatan Oren and Tsvi Piran

The Racah Institute of Physics, The Hebrew University, Jerusalem, Israel, 91904

Abstract

We explore numerically the evolution of a collapsing spherical shell of charged, massless scalar field. We obtain an external Reissner-Nördstrom space-time, and an inner space-time that is bounded by a singularity on the Cauchy Horizon. We compare these results with previous analysis and discuss some of the numerical problems encountered.

1 Introduction

The most general analytic, stationary, and asymptotically flat solution of the Einstein equations is the Kerr-Newman metric, which is characterized by three parameters - mass, charge and angular momentum. The no-hair theorem [1] suggests that at asymptotically late times after the collapse of a massive body to a black hole, the external metric of the black hole relaxes to the Kerr-Newman metric. However, the final state of the inner region is not generally determined and has been the subject of research for some time. Also, it is of interest, especially to gravitational wave astronomers, to predict the specific details of the relaxation of the “hair”.

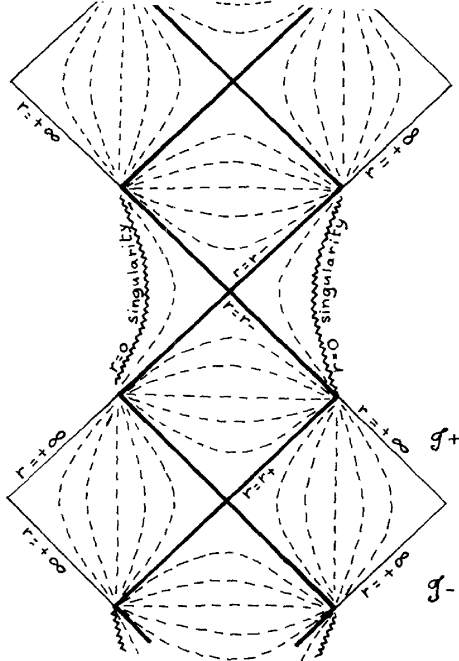


Figure 1: A Penrose diagram for the maximally extended Reissner-Nördstrom space-time. The Cauchy Horizon is marked as $r = r_-$, The Event Horizon as $r = r_+$. Taken from [2].

This appearance of a time-like singularity and a “chain” of asymptotically flat regions in the maximally extended Reissner-Nördstrom metric (Fig.(1)) (and also in the Kerr metric) opened up the discussion of the existence and stability of “wormholes”. The Reissner-Nördstrom metric is problematic as a realistic black hole picture because the part of space-time that lies in the future of the Cauchy Horizon is unpredictable by a set of Cauchy initial conditions given on a space-like surface in the asymptotically flat region. This happens because events in the region beyond the Cauchy Horizon are in causal connection to the time-like singularity.

Consequently we would expect that in a dynamic collapse the space-time will not extend beyond the Cauchy Horizon, but would rather be bounded there by a singularity of some sort. This scenario was predicted by Penrose [3] as early as 1968. The physical mechanism leading to this singularity is known as the “Mass Inflation” scenario [4], and is connected to the infinite blueshift of in-falling radiation on the Cauchy Horizon.

Previous results [5, 6, 7] concerning the stability of the cauchy horizon were acquired either by linear perturbation theory or by numerically evolving a neutral perturbation collapsing on a preexisting Reissner-Nördstrom black hole [8, 9, 10]. The latter model is relatively easy to solve numerically since it does not contain charges and dynamical electromagnetic fields, but on the other hand it does not give the complete picture of the evolution of the black hole and the Cauchy Horizon beginning with a flat space time. Previous work dealing with a fully dynamical charged collapse model [11, 12, 13, 14] focused mainly on the behavior near the origin and outside the horizon, i.e at relatively large values of retarded time but moderate values of advanced time, on the order $10M$. These works indicated that in a charged collapse the Cauchy Horizon is replaced by a weak, null singular segment connected to a space-like singularity at the origin (Fig.(2)). In this work we follow the evolution of a charged matter shell that collapses to form a black hole, and determine the final structure of the inner metric, and the Cauchy Horizon at *large* values of advanced time, deep inside the Black Hole interior.

In section 2, we formulate our basic equations, starting from the gauge invariant Lagrangian of the complex scalar field and casting these equations into the double-null coordinate system. In section 3 we discuss the numerical scheme, its accuracy and the difficulties that arise in this kind of calculation. In section 4 we discuss the numerical results and their implications regarding

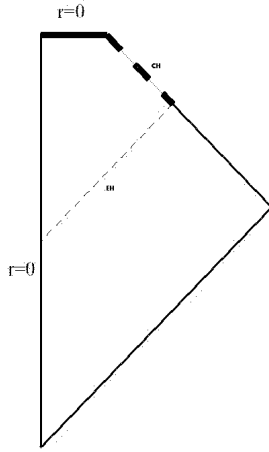


Figure 2: A Penrose diagram for a charged collapse scenario. The dashed lines indicate singularities along the origin and Cauchy Horizon. Taken from [2].

several aspects of black hole physics, such as Mass Inflation, Cosmic Censorship, Wave tails and the No-Hair theorem, and the nature of the Cauchy Horizon singularity.

2 Formulation of the problem

2.1 The equations

We begin with the gauge-invariant Lagrangian for the complex scalar field ψ and the electromagnetic gauge field A_μ [15]:

$$\mathcal{L} = -(\psi_{;a} + ieA_a\psi)g^{ab}(\bar{\psi}_{;b} - ieA_b\bar{\psi}) - \frac{m^2}{\hbar^2}\bar{\psi}\psi - \frac{1}{8\pi}F_{ab}F_{cd}g^{ac}g^{bd}, \quad (1)$$

where we define $F_{\mu\nu} = A_{\nu;\mu} - A_{\mu;\nu}$. We are dealing with a massless field so we will omit the middle term from now on. From this lagrangian we can

derive the Euler-Lagrange equations for the scalar and electromagnetic field, and also the Energy-Momentum tensor to be used in the Einstein equations. The wave equations for the scalar field are:

$$\psi_{;ab}g^{ab} + ieA_a g^{ab}(2\psi_{;b} + ieA_b\psi) + ieA_{a;b}g^{ab}\psi = 0, \quad (2)$$

and its complex conjugate. The Maxwell equations take the form:

$$\frac{1}{2\pi}F_{ab;c}g^{bc} + ie\psi(\bar{\psi}_{;a} - ieA_a\bar{\psi}) - ie\bar{\psi}(\psi_{;a} + ieA_a\psi) = 0. \quad (3)$$

The Energy-Momentum tensor given by:

$$\begin{aligned} T_{ab} = & \frac{1}{2}(\psi_{;a}a\bar{\psi}_{;b} + \bar{\psi}_{;a}\psi_{;b}) + \frac{1}{2}(-\psi_{;a}ieA_b\bar{\psi} + \bar{\psi}_{;b}ieA_a\psi + \bar{\psi}_{;a}ieA_b\psi - \psi_{;b}ieA_a\bar{\psi}) + \\ & \frac{1}{4\pi}F_{ac}F_{bd}g^{cd} + e^2A_aA_b\psi\bar{\psi} + \frac{1}{2}\mathcal{L}g_{ab}. \end{aligned} \quad (4)$$

We choose the (2+2) spherically symmetric, double null coordinate system. The line element in these coordinates can be written as:

$$ds^2 = -\alpha(u, v)^2dudv + r(u, v)^2d\Omega^2, \quad (5)$$

with r being the area coordinate. Note that any coordinate gauge of the form $u \rightarrow f(u), v \rightarrow g(v)$ will preserve the null character of u and v . We will fix this gauge freedom later when discussing the initial conditions.

We need also to fix the gauge freedom of the electromagnetic field A_μ . In our symmetry and coordinate choice the only non-vanishing components of F are $F_{uv} = -F_{vu}$. This means that only A_u and A_v may be non-zero. We can eliminate one of these using the electromagnetic field gauge freedom, $A_\mu \rightarrow A_\mu + \Phi_{;\mu}$, where Φ is an arbitrary scalar function. We choose to eliminate A_v by taking $\Phi = -\int A_v dv$, and so we are left with $A_\mu = (A_u, 0, 0, 0)$. We shall call this quantity $a \equiv A_u$ from now on.

We now proceed to write our equations in an explicit form. We begin with the Maxwell equations. Since we reduced the potential to one component using the gauge freedom, we need only one equation for this field. Eq.(3) is a vector equation with two non-vanishing components u and v , and we may choose either one to evolve the electromagnetic field. We choose the v component, and will use the u component later when checking charge conservation. The v component then becomes (we are using from now on the convention $Z_\mu = \frac{\partial Z}{\partial x^\mu}$):

$$\left(\frac{r^2 a_v}{\alpha^2}\right)_v + \frac{1}{2} i e r^2 \pi (\bar{\psi} \psi_v - \psi \bar{\psi}_v) = 0. \quad (6)$$

We define:

$$q \equiv \frac{2r^2 a_v}{\alpha^2}, \quad (7)$$

and thus separate the 2^{nd} order equation for a into two simpler 1^{st} order equations:

$$\begin{aligned} a_v &= \frac{\alpha^2 q}{2r^2} \\ q_v &= 2\pi i e a r^2 (\psi \bar{\psi}_v - \bar{\psi} \psi_v). \end{aligned} \quad (8)$$

The function $q(u, v)$ defined above is the amount of charge within (i.e. at smaller radii than) a sphere of radius $r(u, v)$ on some space-like hypersurface that contains (u, v) .

The mutually independent elements of $G_{\mu\nu}$ read:

$$\begin{aligned} G_{uu} &= 2 \frac{2\alpha_u r_u - \alpha r_{uu}}{\alpha r} \\ G_{vv} &= 2 \frac{2\alpha_v r_v - \alpha r_{vv}}{\alpha r} \\ G_{uv} &= \frac{\alpha^2 + 4r_u r_v + 4r r_{uv}}{2r^2} \\ G_{\theta\theta} &= 4 \frac{r^2 \alpha_u \alpha_v - r^2 \alpha \alpha_{uv} - \alpha^2 r r_{uv}}{\alpha^4}, \end{aligned} \quad (9)$$

Combining Eq.(9) and the Einstein tensor $G_{\mu\nu}$ we arrive at the field equations:

$$\begin{aligned}
r_{vv} - 2r_v \frac{\alpha_v}{\alpha} + 4\pi r \bar{\psi}_v \psi_v &= 0 \\
r_{uu} - 2r_u \frac{\alpha_u}{\alpha} + 4\pi r (\bar{\psi}_u \psi_u + iea(\psi \bar{\psi}_u - \bar{\psi} \psi_u) + e^2 a^2 \bar{\psi} \psi) &= 0 \\
rr_{uv} + r_u r_v + \frac{\alpha^2}{4} - \frac{\alpha^2 q^2}{4r^2} &= 0 \\
\frac{\alpha_{uv}}{\alpha} - \frac{\alpha_u \alpha_v}{\alpha^2} + \frac{r_{uv}}{r} + \frac{\alpha^2 q^2}{4r^4} + 2\pi (\bar{\psi}_u \psi_v + \bar{\psi}_v \psi_u) + 2\pi iea(\psi \bar{\psi}_v - \bar{\psi} \psi_v) &= 0 \quad (10)
\end{aligned}$$

Finally we evaluate the wave equation and arrive at the form:

$$r\psi_{uv} + r_u \psi_v + r_v \psi_u + iear\psi_v + iear_v \psi + ie \frac{\alpha^2 q}{4r} \psi = 0. \quad (11)$$

We are now in a position to write down the full set of equations to be solved. For this purpose we introduce some new notations:

$$\begin{aligned}
s &\equiv \sqrt{4\pi} \psi \\
w &\equiv s_u ; \quad z \equiv s_v \\
f &\equiv r_u ; \quad g \equiv r_v \quad (12)
\end{aligned}$$

Rearranging and substituting we arrive at the following set of equations:

$$\begin{aligned}
E1 : \quad & rr_{uv} + fg + \frac{\alpha^2}{4} - \frac{\alpha^2 q^2}{4r^2} = 0 \\
E2 : \quad & (ln\alpha)_{uv} - \frac{fg}{r^2} - \frac{\alpha^2}{4r^2} + \frac{\alpha^2 q^2}{2r^4} + \frac{1}{2}(w\bar{z} + \bar{w}z) + \frac{1}{2}iea(s\bar{z} - \bar{s}z) = 0 \\
C1 : \quad & g_v - 2\frac{\alpha_v}{\alpha}g + r\bar{z}z = 0 \\
C2 : \quad & f_u - 2\frac{\alpha_u}{\alpha}f + r\bar{w}w + iea(s\bar{w} - \bar{s}w) + e^2a^2\bar{s}s \\
M1 : \quad & a_v - \frac{\alpha^2 q}{2r^2} = 0 \\
M2 : \quad & q_v - \frac{1}{2}ier^2(s\bar{z} - \bar{s}z) = 0 \\
S : \quad & rs_{uv} + fz + gw + iearz + ieags + ie\frac{\alpha^2 q}{4r}s = 0.
\end{aligned} \tag{13}$$

2.2 The initial conditions

Having specified the equations to be solved we turn to discuss the formulation of the initial conditions. The physical situation we wish to describe is the gravitational collapse of a shell of in-falling charged matter. We choose the domain of integration to be a rectangle in the u - v plane (see section 3.2, where we describe the numerical scheme). We can expect the Event Horizon to be inside the domain of integration, but not the Cauchy Horizon since it is located at infinite null coordinate v (We are not using Kruskal-like coordinates). we can However approach the Cauchy Horizon asymptotically at large values of v .

When we come to specify the metric functions on the initial hypersurface, we must fix the coordinate gauge freedom mentioned in section 2.1. In a Minkowsky space-time we usually choose $u = t - r, v = t + r$. Space-time

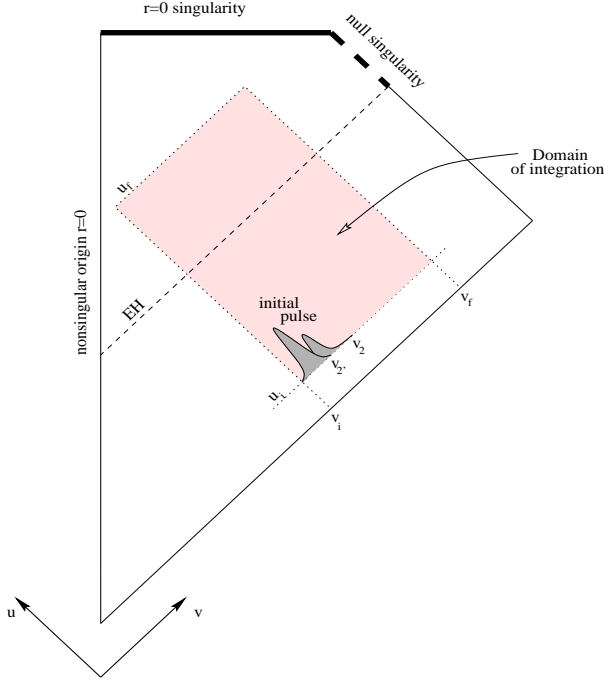


Figure 3: Illustration of the domain of integration in relation to the expected structure of the space-time. The Cauchy Horizon cannot be actually included in the domain because it is in null infinity. Taken from [16]

around a gravitating spherical shell is flat in two regions - inside the shell and at asymptotically large radii. Since we have one constraint equation, C1, that relates r, α and the scalar field on the initial hypersurface, we can choose two of these functions arbitrarily. We would like to take r to be linear with v in order to reflect the fact that we start our integration far from the Event Horizon, where the metric is nearly flat. The fact that this is only an approximation will be pronounced by the deviation of α from its flat-space value. We can further specify the shape of the matter shell on the initial hypersurface, and integrate C1 to obtain α on that surface. Using the

conventional flat-space dependence of r on u and v ,

$$r_i = \frac{v_i - u_i}{2}, \quad (14)$$

we conclude that $g_i = 0.5$, and given an initial distribution of the scalar field that we will soon elaborate on, we get from C1 the following ODE for α :

$$\frac{\alpha_v}{\alpha} = r \bar{z} z. \quad (15)$$

We choose for the initial field distribution a compactly supported function, which is basically one half period of a cosine. Studying equation M2 we see that in order to have a non-vanishing charge distribution we must use for the real and imaginary part of the field two pulses offset in v by some amount. The exact form we choose is:

$$\begin{aligned} Re[s_i] &= \begin{cases} 0 & v_1 > v > v_2 \\ Ar(\frac{1+\cos(\pi \frac{v-v_c}{\Delta v})}{2})^2 & v_1 < v < v_2 \end{cases} \\ Re[s_r] &= \begin{cases} 0 & v'_1 > v > v'_2 \\ Ai(\frac{1+\cos(\pi \frac{v-v'_c}{\Delta v'})}{2})^2 & v'_1 < v < v'_2. \end{cases} \end{aligned} \quad (16)$$

Having specified the two fields r and s on the initial hypersurface, we can analytically derive z and g (which are simply $g = \frac{1}{2}$ and $z = \frac{\partial s}{\partial v}$), and numerically integrate the remaining quantities f, α, a, q and w using equations E1, C1, M1, M2 and S respectively.

We also need to specify the boundary conditions on the ray $v = v_i$. Since the metric on the boundary, which is always inside the collapsing shell, is flat, we can select the conventional flat-space values for the fields there:

$$\begin{aligned} r &= \frac{v_i - u_i}{2} \\ \alpha &= 1 \\ s &= z = q = A = 0 \end{aligned} \quad (17)$$

In selecting these values for the metric functions on the boundary we specify the physical meaning of the metric functions: The choice of α implies that $\frac{u+v}{2}$ is the proper time for an observer located at the origin, while r is the proper surface area of a sphere of a radius $r(u, v)$.

For monitoring the mass content in our space-time we use the mass function,

$$m(u, v) = \frac{r}{2} \left(1 + \frac{q^2}{r^2} + 4 \frac{r_u r_v}{\alpha^2} \right), \quad (18)$$

which represents the total mass in a sphere of radius $r(u, v)$.

3 The numerical scheme

3.1 Domain of integration

The main consideration in choosing the domain of integration is whether or not to include the origin. The origin will be important when discussing critical phenomena [17], however we are only interested in effects that occur at large values of v and at a finite radius, so we can choose the domain to be a rectangle as shown in Fig.(3). The advantage of this approach is that the origin, while being regular, is a coordinate singularity, and this would force us to make a series expansion of the fields near the origin in order to maintain numerical precision.

3.2 Numerical Algorithm

We construct a 2-dimensional grid in the v, u space and integrate in increasing v and u direction. Since our equal-coordinate surfaces lie on the light-cone, there are no Courant-like stability limits on the step size. We implement a Runge-Kutta like scheme by making a trial step to the middle of the cell

and using this information to make a 2nd order full step. We have found this scheme to be simple and efficient.

We use equation E1 to evolve r, f and g . E2 is used to evolve α , and S evolves s, z and w . Finally M1 and M2 evolve a and q respectively. Note, that this scheme is a Free Evolution scheme, since only the dynamical equations are used for evolving the space-time. The constraint equations are used for monitoring the accuracy.

3.3 Adaptive grid refinement

A major problem in black hole numerics is the behavior near the Event Horizon. Although the double-null coordinates we have chosen ensure regularity of the fields even as we cross the horizon, there is nevertheless a fundamental difficulty in following the evolution numerically because of the physical behavior near the Horizon. Consider two outgoing null rays starting at the origin, slightly above and below the Event Horizon. One is destined to escape to infinity while the other will remain trapped inside the Horizon. This means that regardless of how close the two rays were initialii, their distance will diverge as their advanced time v grows. The numerical implication is that the metric function $f = r_u$ diverges along the Event Horizon, and r becomes “discontinuous” asymptotically. If we want to maintain a fixed relative change in the area coordinate r , we have to make the grid denser as we approach the horizon. The step size has to decrease with the distance from the horizon. This decay turns out to be exponential, and the exponent increases as we increase v_{max} . It would be best to change both Δu and Δv as we approach the horizon and reach large values of v , respectively, but we chose in this work to change only Δu because while this is significantly simpler to implement, it gives reasonable results. The choice of having the

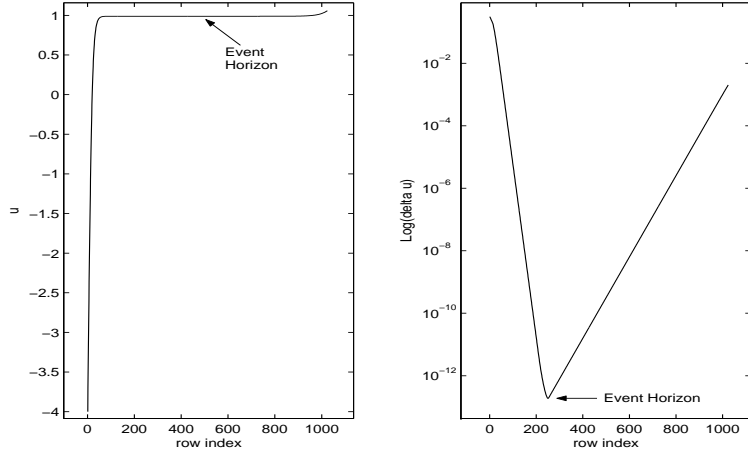


Figure 4: Adaptive grid refinement. The left figure features the development of u along a typical grid, showing how most of the computational effort is concentrated at the neighborhood of the Horizon. The figure on the left is the difference Δu , showing that Δu changes by many orders of magnitude.

refinement algorithm maintain $\frac{\Delta r}{r}$ constant, instead of some other local indicator of accuracy, is not trivial and was made after trial and error indicated that it was the best strategy, and also because r is always finite in the region of interest so it provides a good scale for measuring error. This scheme dictates, for relatively high values of $v_{max} \approx 100M$, a condensation of about 10 orders of magnitude in Δu in the vicinity of the Event Horizon relative to the initial value of Δu . This is illustrative of the difficulty in numerically crossing the Event Horizon at large values of v . Fig.(4) shows an example of the evolution of Δu on a typical space-time.

3.4 Numerical tests

Our first test would have been a comparison of the numerical results with a known analytical solution. Unfortunately, there are no suitable analytical solutions. Therefore, we will have to check our code by other means. We begin with a test of convergence, i.e. we verify that the various fields converge to some value in the expected order of convergence. We evolve the same initial conditions on three grids, g_1, g_2 and g_3 which have fixed grid densities (in both u and v directions) $d_1, 2d_1$ and $4d_1$. We need three grids because we do not know the exact solution, so we can compare only the relative error. In Fig.(5) we plot, for example, the functions $Re[\psi_1 - \psi_2]$ and $4Re[\psi_2 - \psi_3]$. We expect, and verify, that the two curves be nearly but not exactly the same, because higher order terms also have a small contribution to the error. The data in this figure is from a single row($u = const$) but it is representative of the entire grid.

Although convergence is crucial, it still does not guarantee that the results are correct, because if there is an error in the equations, either in the original equations or as they are implemented in the code, the scheme will still converge but to the wrong solution. We are in a unique situation where the constraint equations provide us with a measure of consistency. The Einstein equations preserve the constraints, in the sense that if the initial conditions satisfy the constraint equations, then they will be satisfied also under evolution of the dynamical equations. This is true analytically, but since our solution is numerical we cannot solve exactly either the constraint equations on the initial hypersurface or the dynamical equations through the evolution. Therefore we can only demand that the *error* in the constraint will converge to zero as we make our solution more accurate by condensing the grid, i.e. $C \xrightarrow{stepsize \rightarrow 0} 0$. This is verified in Fig.(6).

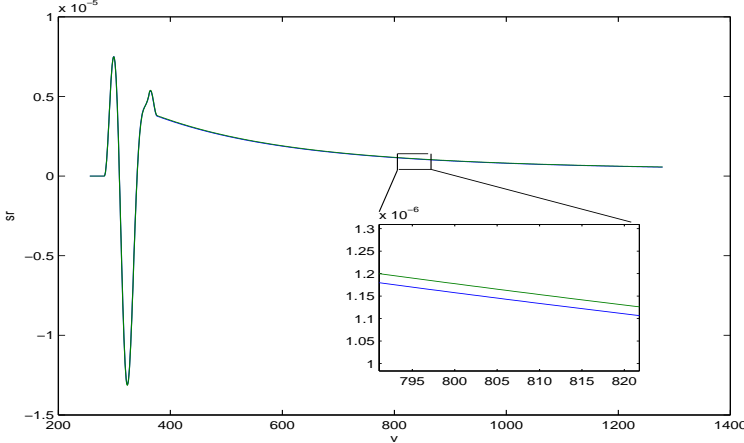


Figure 5: $Re[\psi_1 - \psi_2]$ & $4Re[\psi_2 - \psi_3]$ for the real part of the scalar field on one of the outgoing rays. The two curves are almost indistinguishable, which shows that the scheme converges nicely to 2^nd order

Next we check that our code reproduces known features, such as the location of the horizons, mass and charge conservation etc. Comparing the location of the horizons to the Reissner-Nördstrom solution's $r_{\pm} = M \pm \sqrt{M^2 - q^2}$ we find a correspondence of about one part in 10^5 between the computed and expected radii.

Finally we observe that global mass and charge are conserved. Actually this is not exactly the case since some of the field is scattered by the gravitational and electromagnetic potential as the shell approaches its gravitational radius, but this is in most cases (when $Q < M$) an insignificant amount and the conservation laws seem to hold. Fig.(7) shows the mass M and the charge Q at the last grid-point vs. u . Also shown is Q' which is Q compensated for the charge lost at the last grid point due to outgoing flux:

$$Q'(u) = Q(u) + \int_{u_0}^u r^2(u', v_{max}) Ju(u', v_{max}) du', \quad (19)$$

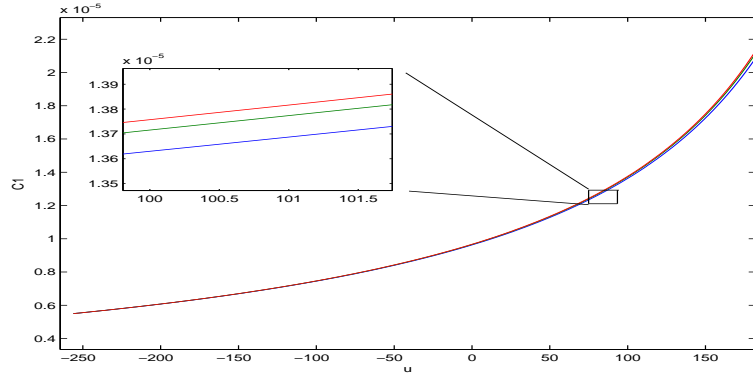


Figure 6: The maximum constraint error along outgoing rays $\max_v(C_1)$, $\max_v(4C_2)$ and $\max_v(16C_3)$ as a function of u on the same 3 grids as in Fig.(5). The three curves are again almost indistinguishable, showing that the constraint violation displays 2nd order convergence to zero. The initial error in the constraint grows with u because of unavoidable accumulation of numerical errors.

which follows from the conservation equation for the electromagnetic current:

$$J^\mu_\mu = 0. \quad (20)$$

It should be noted that the mass inside the domain of integration is not generally conserved, since the reflected waves carry off some mass, as well as charge. The subject of mass conservation is more delicate than charge conservation since the total mass contains also the Energy-Momentum of the gravitational field, which doesn't enter into the Noether current related to the Energy-Momentum tensor. We will refrain from dealing with this topic here.

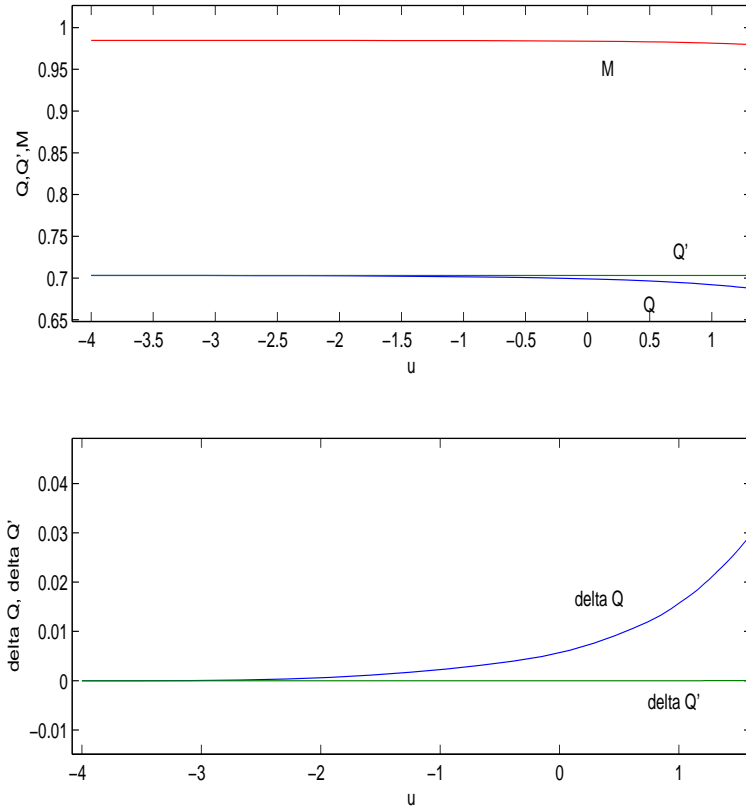


Figure 7: Global charge and mass conservation. Upper figure: Q is the charge $q(u, v)$, Q' is the charge, compensated for the outgoing current density at the last grid point (outgoing flux). Lower figure: the relative change $1 - \frac{Q}{Q_0}$ and $1 - \frac{Q'}{Q_0}$, which is four orders of magnitude smaller.

3.5 Numerical error

To summarize, we can obtain a measure of the relative numerical errors from the tests we discussed. The first test is to use the convergence test and compare the difference in the fields between different grids. There is a difficulty here because this test can only be performed without using adaptive

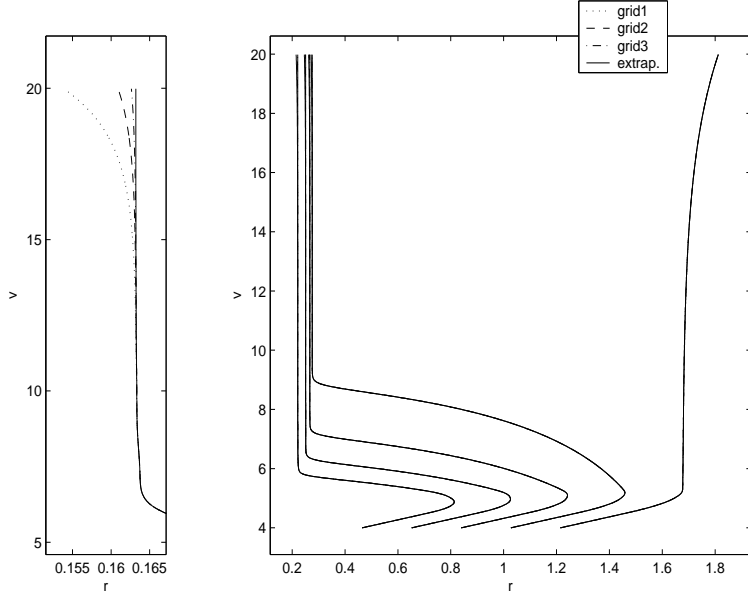


Figure 8: Right panel: The metric function r vs. v for several outgoing null rays, on 3 different grids $g_{1,2,3}$ with grid spacing $4h$, $2h$ and h respectively. The three grids are compared to a solution extrapolated from them, taking into account the 2^{nd} order convergence. This solution is much more accurate than the three others and can be taken to as the “accurate” solution for the purpose of comparison. The 4 curves are almost indistinguishable. Left panel: detail of the leftmost ray

grids. This substantially limits the precision that can be attained in this test, but as Fig.(8) illustrates, even with this limitation we get good results: $\sim 10^{-3}$ maximum relative error. As we indicate in the next paragraph, the error will be lower by an order of magnitude or more if we employ the grid refinement algorithm.

The next test is charge conservation. We can see in Fig.(9) that the

charge conservation error is less than 10^{-4} for the most dense grid. We can also see that the error converges to zero. These results are taken from refined grids, because in this case we are not comparing rows against each other so we don't need to match rows exactly in u value. This test was done with $v_{max} = 20M$. In this case the same calculation on an unrefined grid gave an error larger by an order of magnitude. This ratio will be larger as we increase v_{max} , making the use of grid refinement more and more crucial.

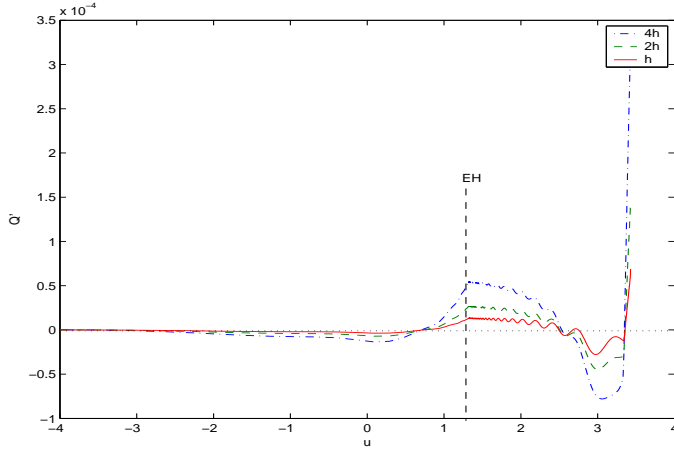


Figure 9: $1 - \frac{Q'}{Q_0}$ for three different grids vs. u . The dashed line indicates the position of the EH. The legend indicates the relative step size used in each grid.

The last test we perform is constraint violation. We can split C1 in Eq.(12) into two terms and compare their relative error:

$$A = g_v - 2\frac{\alpha_v}{\alpha}g \quad (21)$$

$$B = -r\bar{z}z. \quad (22)$$

Now we can take $\frac{|A|-|B|}{|A|+|B|}$ to be the relative error. However there is a problem since $|A| + |B|$ has no definite scale and it often intersects zero, so the error

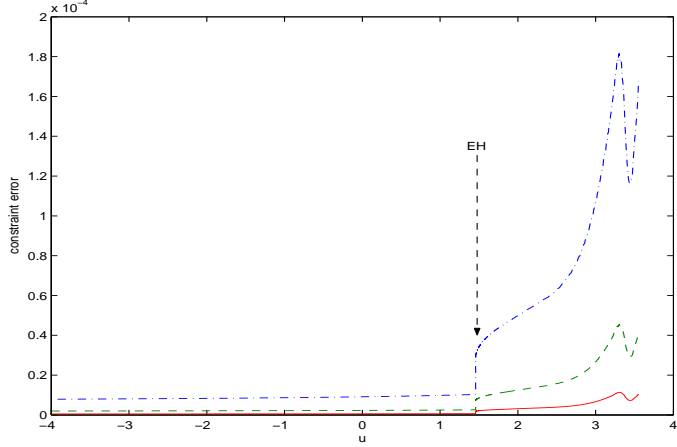


Figure 10: The relative error in the constraint, $\max_v \left(\frac{A-B}{\sqrt{\langle (A+B)^2 \rangle_v}} \right)$ vs. u . The three curves are for the same 3 grids as in Fig.(8).

behaves very badly. Therefore we will compare $(A - B)$ in each $u = \text{const}$ segment to the r.m.s. of $(A + B)$ along the same segment. The results are given in Fig.(10), and show a maximum error level of $\sim 10^{-5}$ in the finest grid used.

4 Results

4.1 Formation of the black hole

We begin Fig.(11) with a null-ray diagram giving an overview of the space time. The diagram shows the formation of an Event Horizon and then a Cauchy Horizon at asymptotically large v . Looking closely at the null rays approaching the Cauchy Horizon we see that it is not stable, as the asymptotic ($v \rightarrow \infty$) value of r decreases as u increases. Finally at large enough values of u the rays reach the origin ($r = 0$), which signals the appearance

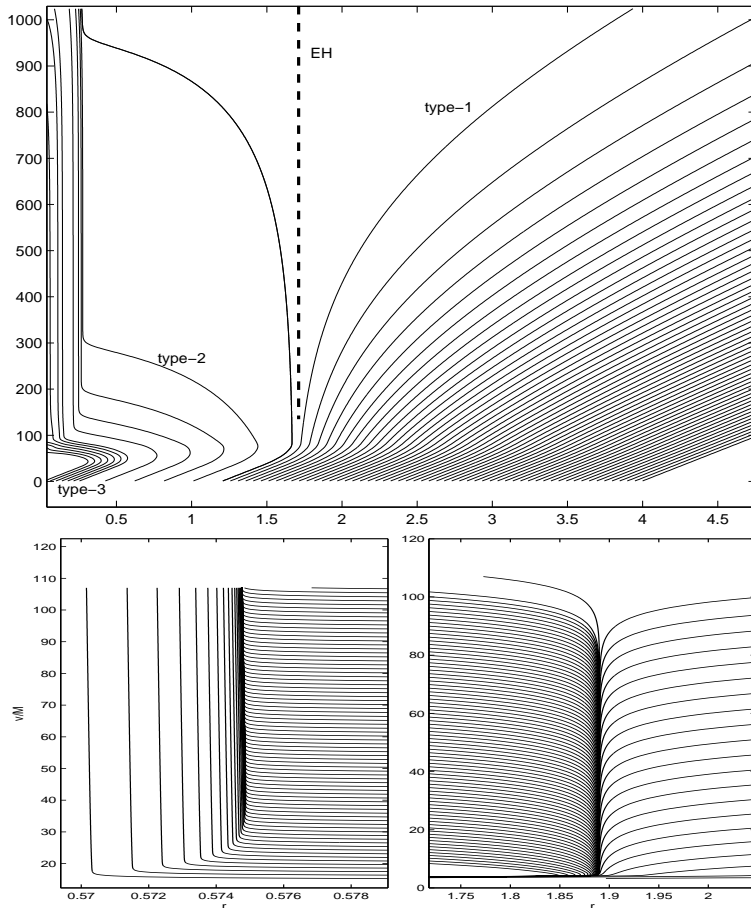


Figure 11: Null rays. The top figure shows the entire domain of integration, and the three classes of rays: type-1 rays reach null-infinity, type-2 approach the Cauchy Horizon and type-3 terminate at the singular origin. The dashed line signifies the approximate location of the Apparent Horizon. the two lower figures focus on the vicinities of rays approaching the Cauchy Horizon (left) and the Event Horizon (right).

of a space-like singularity.

4.2 charge Dynamics

The Cosmic Censorship conjecture [18] states that all singularities in nature are contained within an Event Horizon , so there are no “Naked singularities”. It follows from this that it is impossible to overcharge a black hole (i.e. to increase its charge-to-mass ratio above 1) since there is no black hole solution with this ratio. It is interesting to check if this holds in our collapse scenario by increasing the initial charge of the collapsing shell. It can be seen in Fig.(12) that, for a certain initial configuration, as we increase the coupling constant e , and with it the initial charge to mass ratio, the final black hole charge to mass ratio reaches a maximal value smaller than 1 and then decreases. The physical mechanism that causes this behavior is the electrostatic repulsion of the outer parts of the shell, which increases relative to the gravitational pull they experience as the charge increases, and causes them to be reflected back towards large radii at the early stages of the

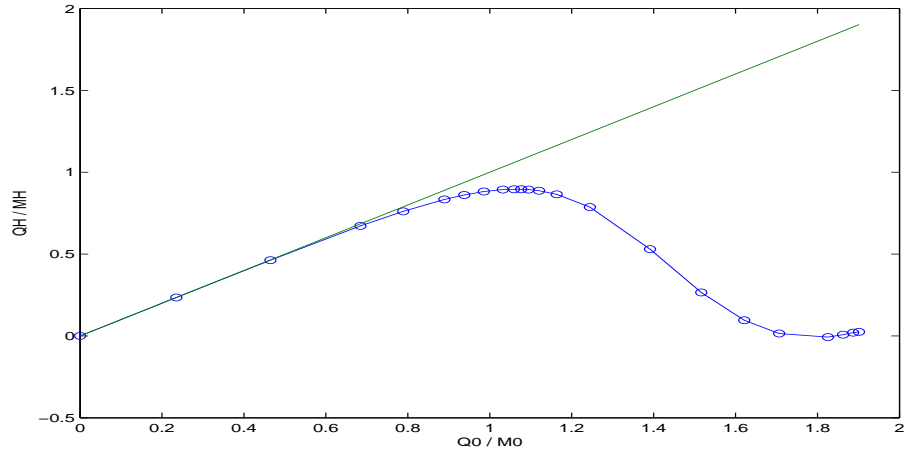


Figure 12: The charge to mass ration on the Event Horizon for different initial conditions.

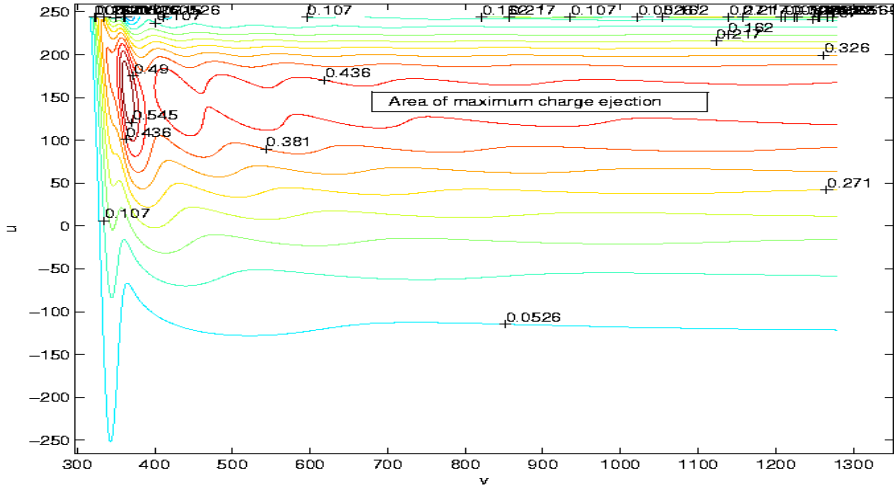


Figure 13: The dynamical ejection of excess charge. Most of the charge is removed well before the shell reaches the horizon (upper edge, $u \approx 250$), at $u \approx 150$.

collapse and radiate part of the initial charge away. This can be understood as a scattering process, where at each instant in time the shell encounters some potential barrier with certain reflection and transmission coefficients. As long as the charge-to-mass ratio will be greater than unity, no horizon will form, and charged matter will be able to escape. Ordinarily the charge and mass become equal some finite time before the shell crosses its gravitational radius and a Horizon forms, so the final charge-to-mass ratio decreases further and ends up smaller than unity.

This process can be seen by inspecting the movement of charges on the computational grid. The outgoing current density, in our coordinates, is proportional to the u component of the 4-current J_μ . Note that this is a matter of interpretation since normally the charge density would be the time-like component of the 4-current, and the current density would be the space-

like component. In our coordinate system u and v are both null, but we treat v and u as the “spatial” and “temporal” coordinates because we are dealing with an in-falling shell. Fig.(13) shows a contour of this quantity for the case $\frac{Q_0}{M_0} = 1.7$.

4.3 Wave tails

Next we observe the mechanism behind the No-Hair theorem, mentioned in chapter 1. We inquire how the black hole radiates away the “hair”, i.e. any feature of the collapsing matter except it’s charge, mass and angular momentum. We want to compare this decay to theoretical results predicting a certain power law decay of the tails at late times. Note that we perform this analysis along the Event Horizon, which is a null hypersurface with a constant radius. Hod&Piran [13] predicted in this case the following behavior on the Horizon:

$$\psi \sim e^{i\frac{eQ}{r_+}} v^{-\beta} ; \quad \beta = 1 + \sqrt{(2l+1)^2 - 4(eQ)^2}, \quad (23)$$

where l is the multipole moment of the scalar perturbation. In our case $l = 0$ because we deal with spherical symmetry. The first term in Eq.(23) is an oscillation term with angular frequency $\frac{eQ}{r}$. The second term is a power-law decay of the field magnitude. Typically the field magnitude on the horizon begins to decay with Quasi-Normal ringing (exponentially decaying oscillations) which decays exponentially, Then the power-law tail sets in and continues to asymptotically large advanced time v where it dominates the behavior of the field. This can be clearly seen in Fig.(14).

The above expression for the oscillation and power law index were checked over a range of the parameter eQ , by changing e and leaving all other parameters constant. The results in Fig.(15) show good correspondence with

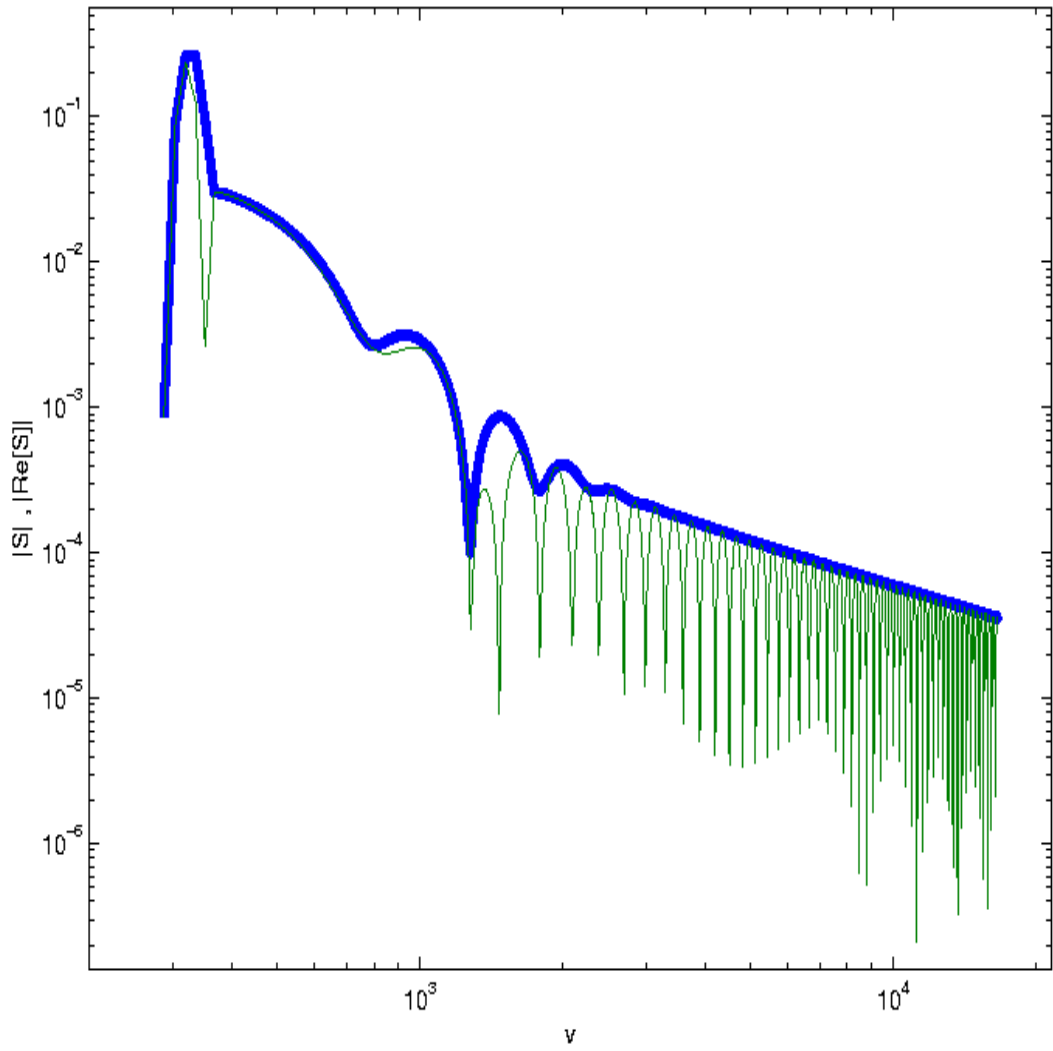


Figure 14: A typical configuration of the scalar field amplitude on the horizon, showing Quasi-Normal ringing followed by a power-law decay (the “tail”). The thick line is the amplitude of the field, the thin line is the absolute value of the real part of the field.

both terms in Eq.(23).

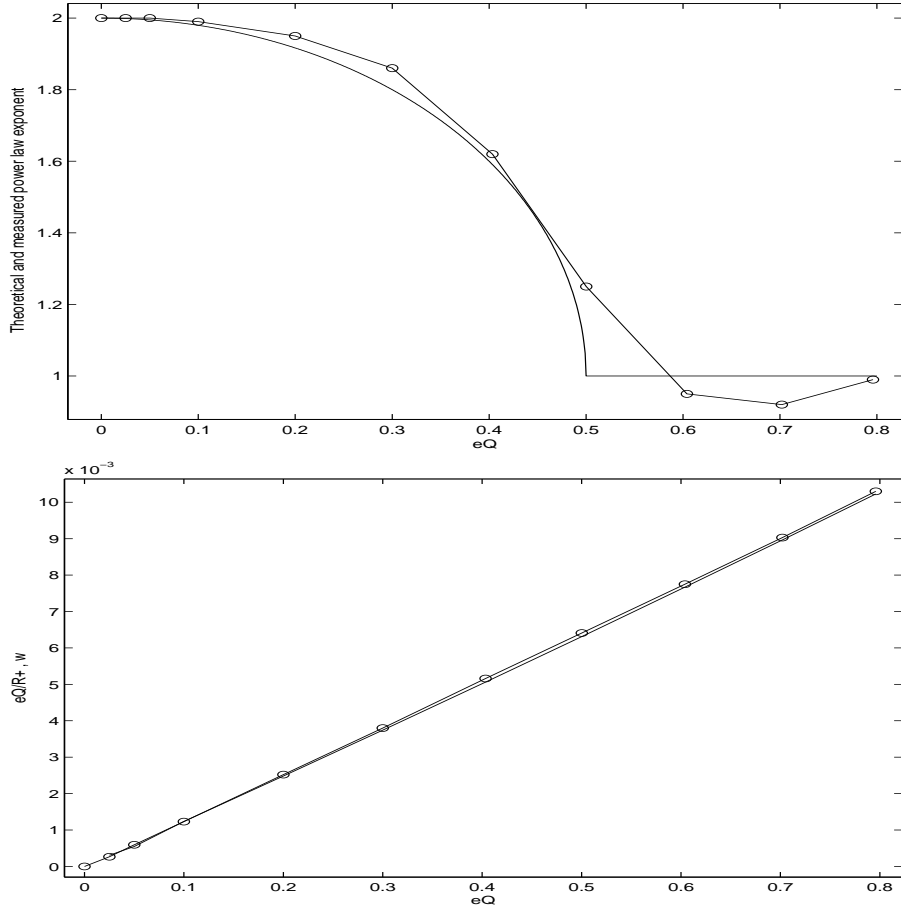


Figure 15: Upper figure: The real part of the power law index for spherical charged perturbations versus the theoretical prediction. Lower figure: The phase oscillation frequency versus the theoretical value, $\frac{eQ}{r^+}$.

4.4 The Cauchy Horizon

We now turn to examine the behavior of the space-time near the Cauchy Horizon. First we try to verify that null rays of type-2 actually reach an

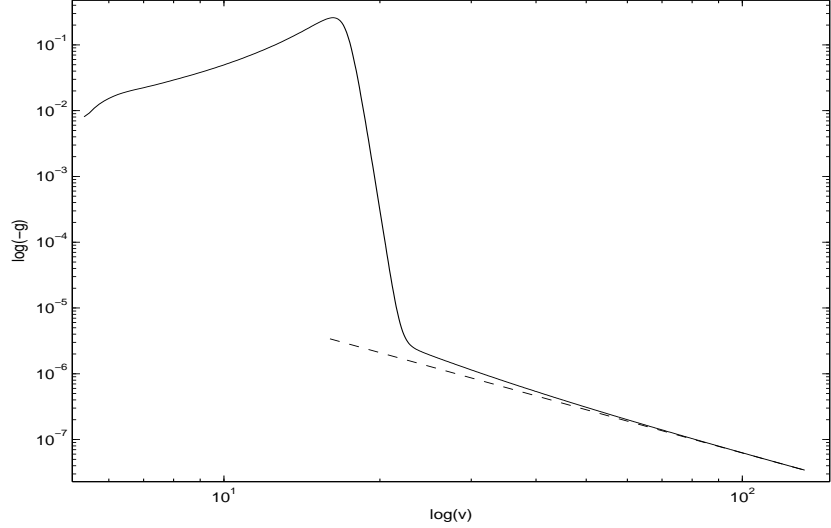


Figure 16: The behaviour of r_v along a null ray approaching the Cauchy Horizon . The power-law decay can be seen clearly at late times.

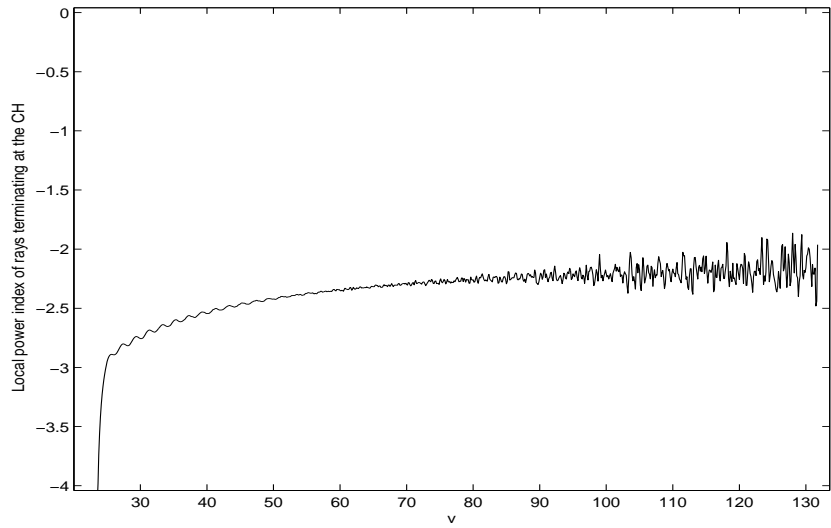


Figure 17: The local power-law index of r_v at the approach to the Cauchy Horizon . r_v behaves like v^{-2} at large v , signifying that r itself approaches a constant value as v^{-1} . The noise at large v is only a numerical artifact.

asymptotically fixed radius, rather than assuming a course that would ultimately bring them, at very large values of v , to the origin. In order to do this we must extend our domain of integration, so that we can observe the decay of r_v over at least one order of magnitude and establish the asymptotic behavior. In Fig.(17) and Fig.(17) such an analysis is made, showing that $r_v \sim v^{-2}$. This confirms the existence of a Cauchy Horizon.

The next thing we want to know is whether the Cauchy Horizon is singular, and if so how much. One indication of a singularity is an exponential divergence of the mass function. This can be seen in Fig.(18), for a typical space-time. This divergence is dominated by an exponential decay of α with v , which makes the mass function diverge exponentially, because it depends on α as α^{-2} . This can be interpreted physically as an infinite blue-shift of in-falling radiation at the Cauchy Horizon, since α is also g_{tt} if we shift to a time-space (1+3) coordinate frame. The theoretical prediction for mass-inflation is $m \sim e^{\kappa v}$, where κ is the surface gravity on the inner horizon. For a static Reissner-Nördstrom black hole this is given by [9] Eq.(24), and it agrees numerically to about 10 – 20% with the measured exponent.

$$\kappa = \frac{\sqrt{1 - (\frac{Q}{M})^2}}{(1 - \sqrt{1 - (\frac{Q}{M})^2})^2}. \quad (24)$$

The singularity also manifests itself in the Ricci curvature scalar, R . The Ricci scalar is a purely geometrical entity, which can be written only with the metric functions and their derivatives. However, we can use our dynamical equations to express this quantity through the physical fields in the problem. We arrive at this form:

$$R = -\frac{4}{\alpha^2}[(\bar{w}z + w\bar{z}) + iea(s\bar{z} - \bar{s}z)]. \quad (25)$$

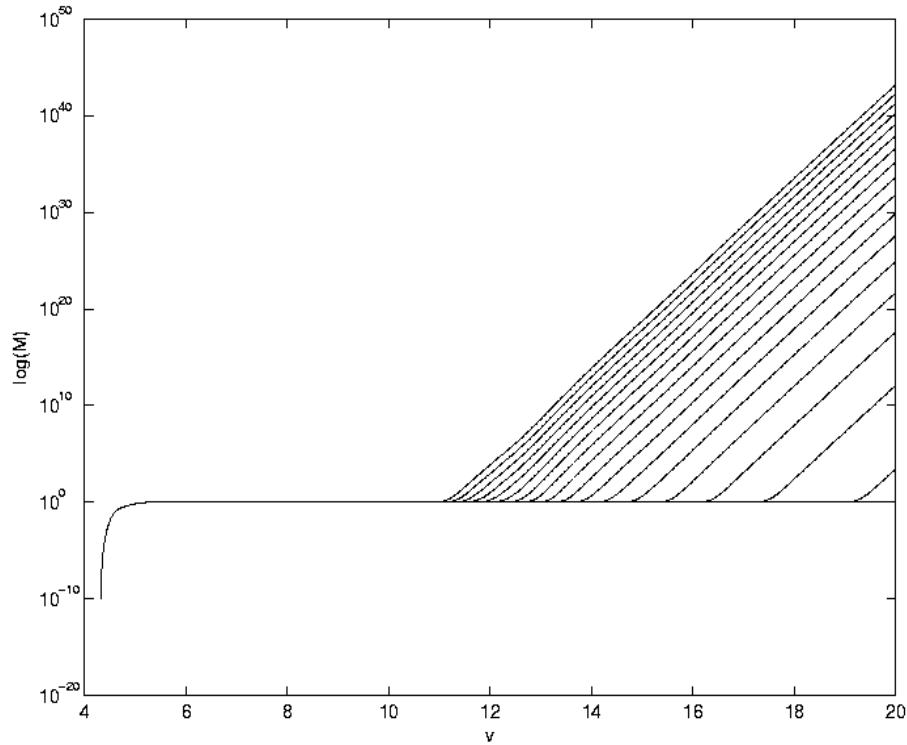


Figure 18: Mass inflation near the CH. Each curve is for a constant u , u is increasing from lower to higher lines.

R can be seen to diverge exponentially on the horizon while oscillating at some definite frequency (see Fig.(19)). This behavior indicates the existence of some kind of curvature singularity, but does not tell us if it is strong or weak, i.e. if the tidal forces felt by an observer crossing it are infinite or finite. The divergence in R is caused by the exponential decay of α , and the oscillation is caused by the oscillatory behavior of the scalar field. We can observe the frequency of this oscillation by looking at $R\alpha^2$ which contains the oscillating term without the exponential divergence. Fig.(20) shows this oscillation and it's Fourier transform. A strong oscillation with period 0.5M

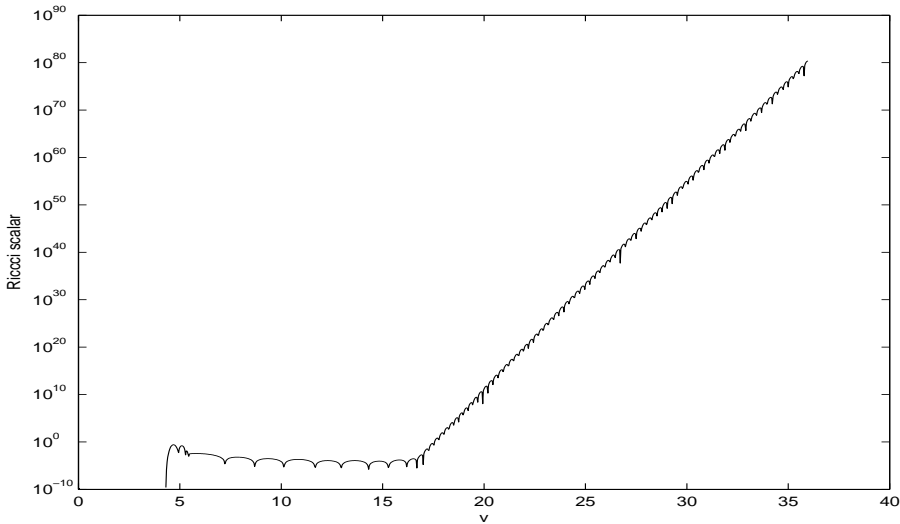


Figure 19: The Ricci scalar on an outgoing null ray intersecting the Cauchy Horizon. The cusps indicate points where R changes sign.

is accompanied by a weaker component with period $0.6M$, and an oscillation with “beat” is produced.

It is interesting to note here, that as the curvature radius at the Horizon of a black hole is on the order of magnitude of it’s gravitational radius, which is $\sim 10^4 m$ for a solar mass black hole, and the planck scale is $\sim 10^{-35} m$, the Ricci curvature can grow by approximately 40 orders of magnitude before it reaches Planckian scales. This means that our analysis brings us well into the Plackian regime, where classical GR begins to fail.

5 Summary and conclusions

We have developed a numerical code that solves the coupled Einstein-Maxwell equations in a dynamical collapse situation. This has enabled us to explore phenomena involved in black hole formation that was previously handled by

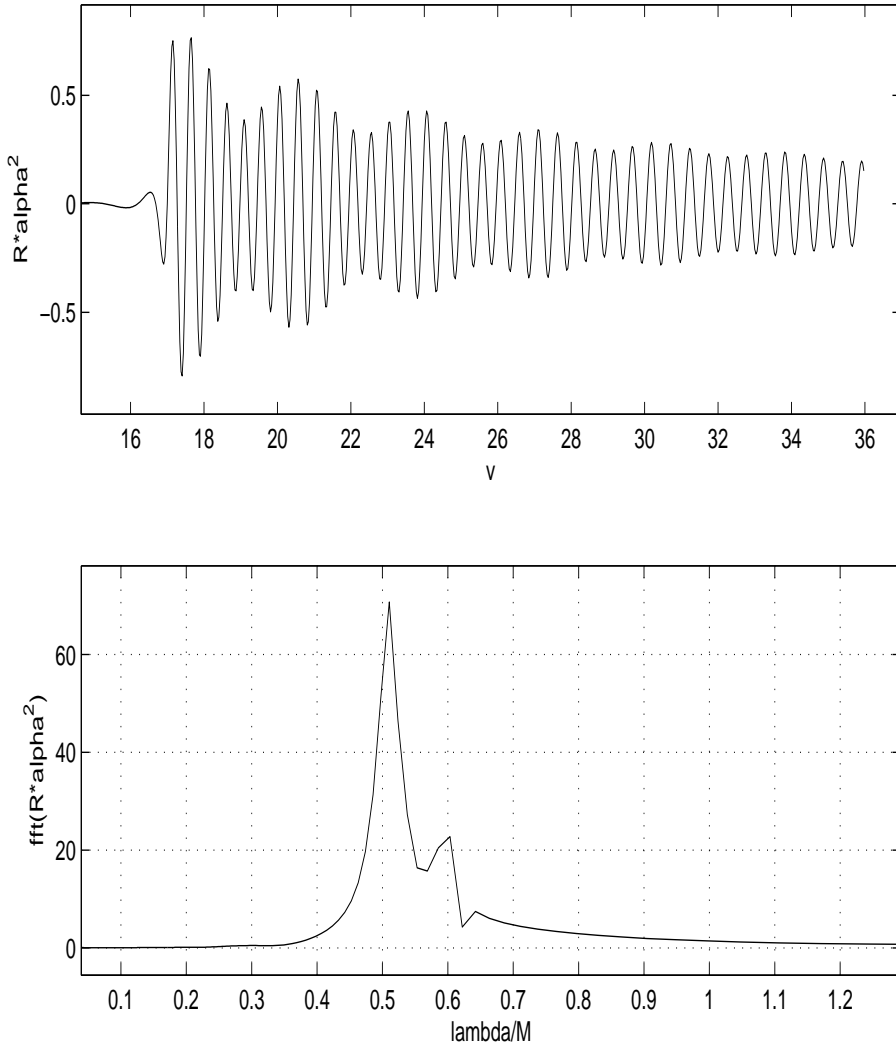


Figure 20: The oscillatory part of the Ricci scalar. Top panel shows an oscillation with a weak ‘beat’. The bottom panel shows the Fourier transform of the curve in the top panel.

analytic or numerical perturbative analysis. The difficulty in this kind of numerical code is in maintaining small numerical errors in spite of extreme gradients near the Event Horizon. We have solved this problem by using a

non-uniform grid that covers the difficult areas with dense grid points. The scheme was shown to converge and give results accurate to better than than 1 part in 10^3 , even in areas deep inside the black hole.

We have shown that in a dynamical collapse of charged matter, some of the charge is radiated away because of electrostatic repulsion and scattering on the gravitational potential. This is in accord with the Cosmic Censorship conjecture which forbids the charge in the Black Hole to surpass it's mass. We also observed the radiative tails that are left on the Horizon after the black hole is formed. These were shown to have the well known structure of an initial decaying oscillation (Quasi-Normal ringing) followed by a power law decay that continues asymptotically.

Finally we ventured deep inside the black hole interior and examined the properties of the inner Horizon. We have found that before being completely destroyed and turning into a strong space-like (i.e. Schwarzschild-like) singularity it behaves as a weak, null singularity. Since the Cauchy Horizon is located at $v = \infty$ in our scheme we cannot reach it by numerical evolution. However physically it is reached in a finite proper time by an in-falling observer (This is true since $\alpha^2(u, v)dt$ which is the proper time differential for an observer at (u, v) decays exponentially as $v \rightarrow \infty$, giving a finite lapse of proper time until reaching the Cauchy Horizon). The weakness of the singularity thus leaves open the question of the traversability of the “Kerr Tunnel”, making it unclear wether it is physically possible for matter to cross the CH into a another asymptotically flat region.

References

- [1] R. Ruffini and J. A. Wheeler, Physics Today **24**, 30 (1971); C. W. Misner, K. S. Thorne and J. A. Wheeler, Gravitation (Freeman, San Francisco 1973).
- [2] B. Carter, in black holes, 1972 Les Houches meeting, C. DeWitt, Gordon and Breach science publishers.
- [3] R. Penrose, in Battelle Rencontres, edited by C. de Witt and J. Wheeler (W. A. Benjamin, New York, 1968), p. 222. Letters v.482, p.L139.
- [4] E. Poisson and W. Israel, Phys. Rev. **D41**, 1796 (1990).
- [5] W. A. Hiscock, Phys. Lett. **A83**, 110 (1981).
- [6] A. Ori, Phys. Rev. Lett. **67**, 789 (1991).
- [7] A. Ori, Phys. Rev. Lett. **68**, 2117 (1992).
- [8] R.S. Hamadé and J.M. Stewart, Class. Quantum Grav. **13**, 497 (1996).
- [9] P. R. Brady and J. D. Smith, Phys. Rev. Lett. **75**, 1256 (1995).
- [10] Lior M. Burko and Amos Ori, Phys.Rev. D56 (1997) 7820-7832
- [11] S. Hod and T. Piran, Phys. Rev. D 58, 024017 (1998).
- [12] S. Hod and T. Piran, Phys. Rev. D 58, 024018 (1998).
- [13] S. Hod and T. Piran, Phys. Rev. D 58, 024019 (1998).
- [14] S. Hod and T. Piran, Phys.Rev.Lett. 81 (1998) 1554-1557

- [15] S.W. Hawking and G.F.R. Ellis, *The Large Scale Structure of Space-Time*, Cambridge University Press 1973.
- [16] E. Sorkin and T. Piran, Phys.Rev. D63 (2001) 084006 .
- [17] M.W. Choptuik, Phys. Rev. Lett. 70, 9-12 (1993).
- [18] R. Penrose, Riv. Nuovo Cimento I 1, 252 (1969); R. Penrose in General Relativity, an Einstein Centenary Survey, eds. S. W. Hawking and W. Israel (Cambridge University Press, 1979).